Electronic Supplementary Information

Functional and structural insight into lignocellulosic fibers for high-areal-capacity lithium–sulfur batteries

Jong Hyuk Yun,[a] Joo-Hyung Kim,[b] Pitchai Ragupathy,[c] Dong Jun Kim[d,*] and Do Kyung Kim[a,*]

[a]Department of Materials Science and Engineering, Korea Advanced Institute of Science and Technology (KAIST), 291 Daehak-ro, Yuseong-gu, Daejeon 34141, Republic of Korea

[b]School of Materials Science and Engineering, Gyeongsang National University, 501 Jinjudaero, Jinju 52828, Republic of Korea

[c]Electrochemical Power Sources Division, Central Electrochemical Research Institute (CECRI), Karaikudi-630 003, India

[d]School of Chemistry, University of New South Wales, Sydney, NSW 2052, Australia

* Corresponding authors.

E-mail addresses: dongjun.kim@unsw.edu.au (D. J. Kim), dkkim@kaist.ac.kr (D. K. Kim)

Table S1. Assignments of Fourier-transform infrared spectroscopy (FT-IR) peaks. The raw hemp fiber, degummed hemp fiber, and hydrothermally carbonized hemp fiber.

Wavenumber (cm^{-1})	**Chemical structure**	**References**
3338	O–H	44, 45
2917	C–H	44, 45
1701	Non-conjugated carbonyl (C=O)	44
1633	Conjugated C=O	46
1610, 1508	Aromatic ring	45–47
1380	C–C, C–H of syringyl (S) unit in lignin	46, 48
1211	C–C, C–O of guaiacyl (G) unit in lignin	46, 49
1025	Cellulose	48
834	p-hydroxyphenyl (H) unit in lignin	46

Table S2. The I_D/I_G ratio of Raman spectroscopy. The I_D/I_G ratio of *C*400-Hemp, *C*500-Hemp, *C*600-Hemp, *C*700-Hemp, and *C*800-Hemp, calculated from Raman spectroscopy.

Sample	I_D/I_G ratio
***C*400-Hemp**	0.686
***C*500-Hemp**	0.741
***C*600-Hemp**	0.773
***C*700-Hemp**	0.881
***C*800-Hemp**	0.959

Table S3. R_o, R_{SEI}, and R_{ct} values from the fitted Nyquist plot of electrochemical impedance spectroscopy (EIS). The pristine and cycled cells were analyzed by EIS with the sulfur loading of 5.12 mg cm^{-2}.

	R_o (Ω)	R_{SEI} (Ω)	R_{ct} (Ω)
***S*-Hemp**	4.8	—	35.0
***S*-Hemp_cycled**	6.8	5.2	4.7
***S*-Hemp@VO_2**	4.8	—	29.0
***S*-Hemp@VO_2_cycled**	6.9	2.7	2.6

Table S4. The current densities of the individual peaks from cyclic voltammetry. The magnitude of peak current density on each cathodic (C1, C2) and anodic (A1) peaks varying the scan rates (0.05, 0.1, 0.2, 0.3 mV s^{-1}), obtained from CV measurement of *S*-Hemp and *S*-Hemp@VO_2.

***S*-Hemp**

Peak current (mA) / Scan rate	C1	C2	A1
0.05 mV s^{-1}	1.31	3.04	3.05
0.1 mV s^{-1}	1.94	4.05	4.75
0.2 mV s^{-1}	2.87	5.26	6.41
0.3 mV s^{-1}	3.57	6.06	7.60

***S*-Hemp@VO_2**

Peak current (mA) / Scan rate	C1	C2	A1
0.05 mV s^{-1}	1.61	3.66	4.12
0.1 mV s^{-1}	2.37	4.85	5.88
0.2 mV s^{-1}	3.20	5.98	7.55
0.3 mV s^{-1}	4.04	7.07	8.69

Table S5. Diffusivity of lithium. The diffusivity of lithium ($cm^2\ s^{-1}$) calculated by Randles-Sevcik equation on each cathodic (C1, C2) and anodic (A1) peaks varying the scan rates (0.05, 0.1, 0.2, 0.3 mV s^{-1}), obtained from CV measurement of *S*-Hemp and *S*-Hemp@VO_2.

S-Hemp

Diffusivity of Lithium ($cm^2\ s^{-1}$) / Scan rate	C1	C2	A1
0.05 mV s^{-1}	2.31×10^{-8}	1.26×10^{-7}	1.26×10^{-7}
0.1 mV s^{-1}	5.11×10^{-8}	2.23×10^{-7}	3.05×10^{-7}
0.2 mV s^{-1}	5.58×10^{-8}	3.75×10^{-7}	5.58×10^{-7}
0.3 mV s^{-1}	5.75×10^{-8}	1.66×10^{-7}	2.61×10^{-7}

S-Hemp@VO_2

Diffusivity of Lithium ($cm^2\ s^{-1}$) / Scan rate	C1	C2	A1
0.05 mV s^{-1}	7.02×10^{-8}	3.63×10^{-7}	4.60×10^{-7}
0.1 mV s^{-1}	7.61×10^{-8}	3.19×10^{-7}	4.68×10^{-7}
0.2 mV s^{-1}	6.95×10^{-8}	4.86×10^{-7}	7.73×10^{-7}
0.3 mV s^{-1}	7.39×10^{-8}	2.26×10^{-7}	3.42×10^{-7}

Table S6. Metrics of high-areal-capacity Li–S cell configurations based on carbonaceous fabrics as cathode materials. The mass of anode for all cells was supposed as 16.44 mg (14 mm disk, 250 μm), and the voltage of all cells was equalized as 2.1 V. The mass of separator was neglected**.**

Ref.	Material	S loading (mg cm^{-2})	Areal capacity (mAh cm^{-2})	Current density (mA g^{-1})	Mass of cathode (mg)	Mass of electrolyte (mg)	Area of cathode (cm^2)	Energy density (Wh kg^{-1})	Power density (W kg^{-1})
This work	***S*-Hemp@ VO_2**	15.36 5.12	14.8 5.8	167.5 1675	43.97 14.65	229.1 76.4	1.13	121.4 128.2	18.7 167.6
25	Stacked CNT-S paper	17.3	15.1	83.75	43.33	302.3	1.33	116.3	8.4
26	SWCNT film	7.2	8.63	167.5	8.47	113.2	1.13	148.5	18.3
29	LRC/S@ FEG	10.8	10.7	111.67	20.22	970.9	0.79	17.5	2.5
30	HCFF-S	16.5	16.3	167.5	39.10	445.7	1.00	68.3	11.6
31	Layer-by-layer PCNF	11.4	11.3	335	24.86	225.5	0.79	69.9	30.1

Table S7. List of chemical species detected at particular wavenumbers obtained from operando Raman spectroscopy.

Wavenumber (cm^{-1})	**Species**	**Reference**
200, 445	S_4^{2-}	64, 66
219, 477	S_8	65
280	Electrolyte	65, 66
362	S_8^{2-}	65
390–400	S_7^{n-}, S_8^{n-}	65, 66
505	S_4^{-}	65, 67
748	LiTFSI	65, 66
575, 1024, 1127, 1171	$S_2O_3^{2-}$	68, 69

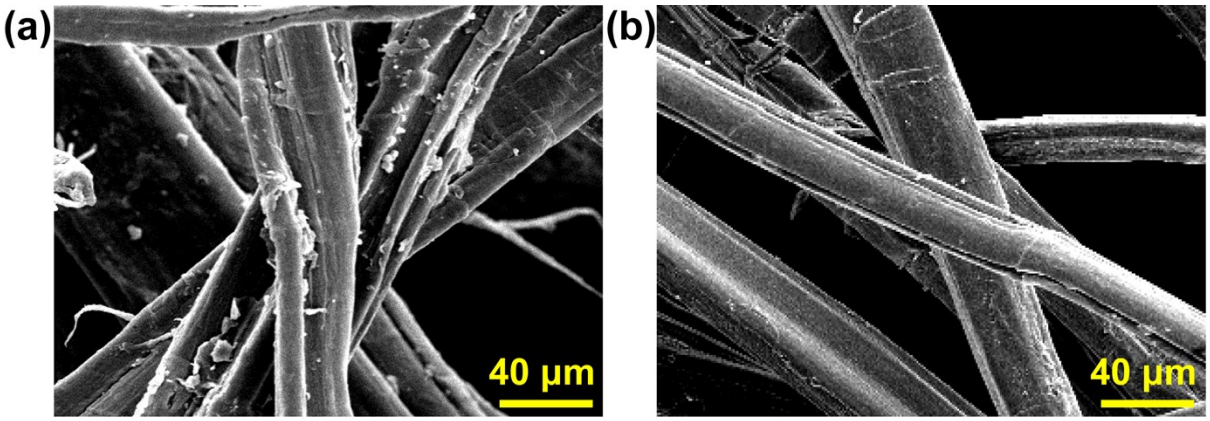

Fig. S1. SEM images of hemp derivatives. (a) raw hemp fiber and (b) degummed hemp fiber, demonstrating thick and smooth morphology where the bundle of internal fibers are unexposed.

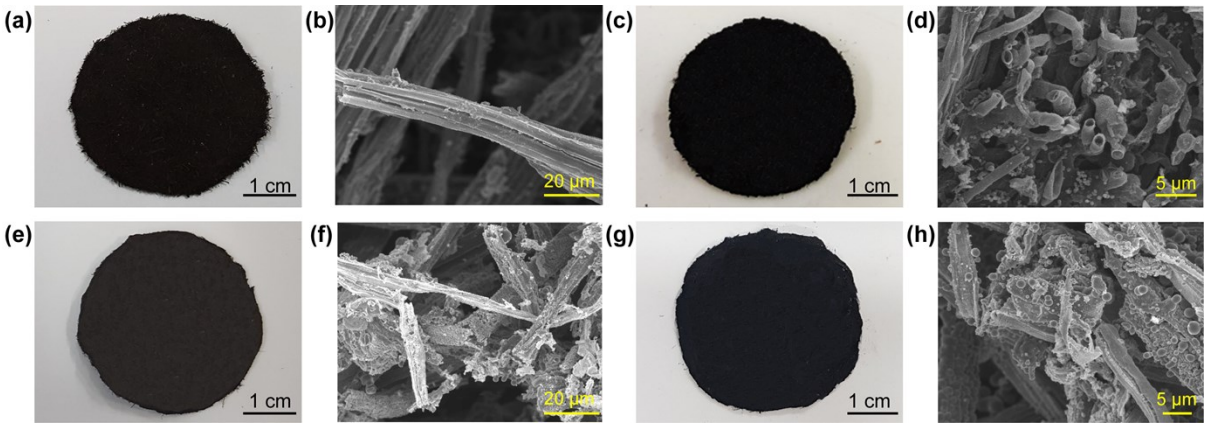

Fig. S2. Digital photographs and SEM images of the fabricated sheets. (a,b) hydrothermally carbonized raw-hemp fiber, (c,d) CO_2-activated raw-hemp fiber, (e,f) hydrothermally carbonized degummed-hemp fiber, and (g,h) CO_2-activated degummed-hemp fiber. Digital photographs show all the sheets maintain the self-stacked form. In terms of microstructure, hydrothermally carbonized raw-hemp fiber sheet demonstrates the bundle of vessels (Fig. S2b), and CO_2-activated raw-hemp fiber sheet shows interwoven carbon micro-tubes split from the bundle of vessels (Fig. S2d). However, the fiber in degummed-hemp fiber sheet (Fig. S2f,h) do not maintain a rigid vascular structure both after hydrothermally carbonized and CO_2-activated, due to the absence of lignin.

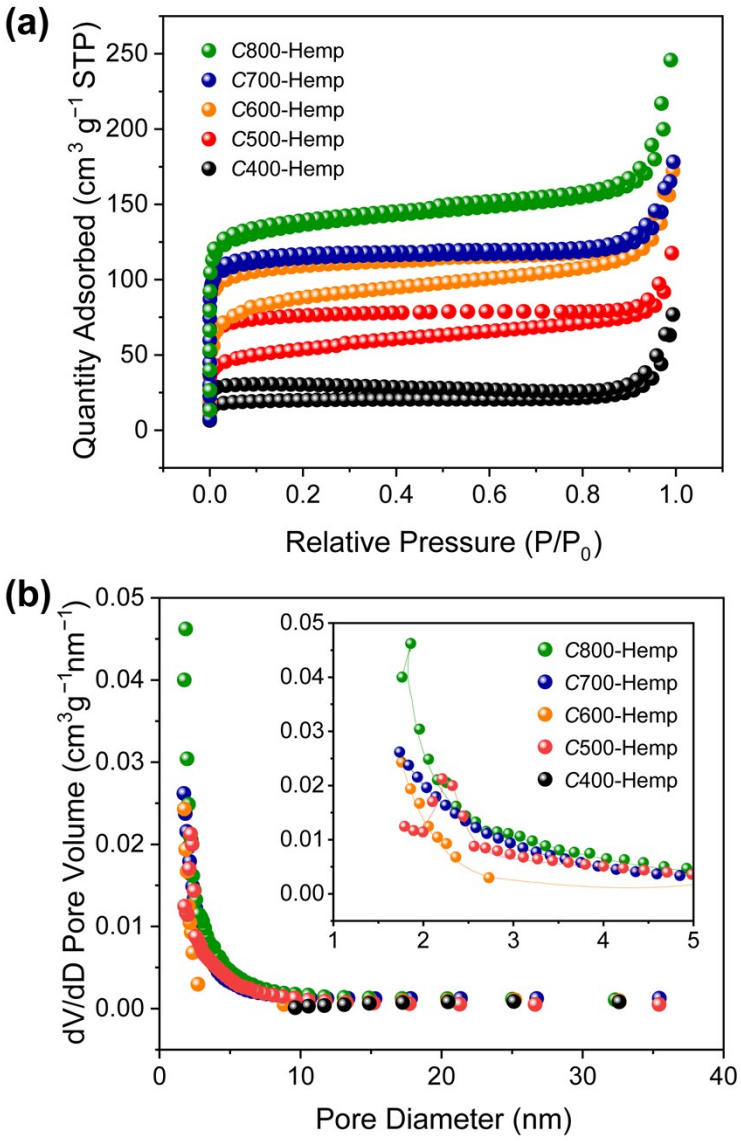

Fig. S3. Porosity measurement of hemp fibers. (a) BET adsorption-desorption isotherm linear plot and (b) pore distribution obtained from BJH adsorption dV/dD pore volume of CO_2-activated hemp fibers varying the temperature of 400ºC, 500ºC, 600ºC, 700ºC, and 800ºC (denoted as *C*400-Hemp, *C*500-Hemp, *C*600-Hemp, *C*700-Hemp, and *C*800-Hemp).

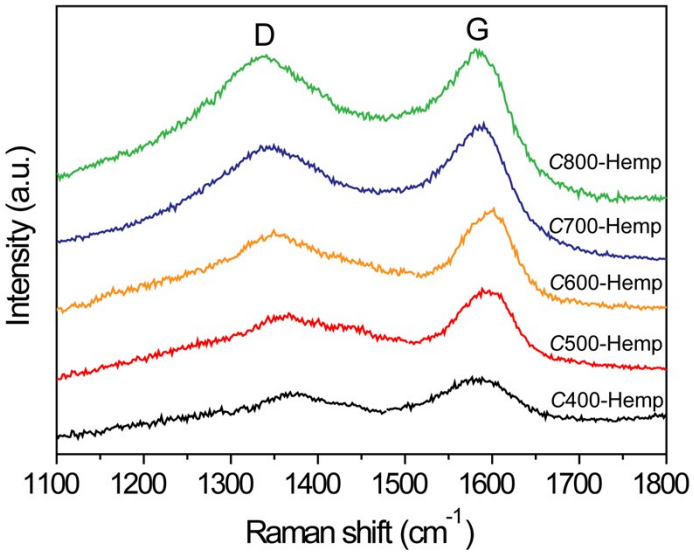

Fig. S4. Temperature dependent Raman spectra. The Raman spectra of *C*400-Hemp, *C*500-Hemp, *C*600-Hemp, *C*700-Hemp, and *C*800-Hemp.

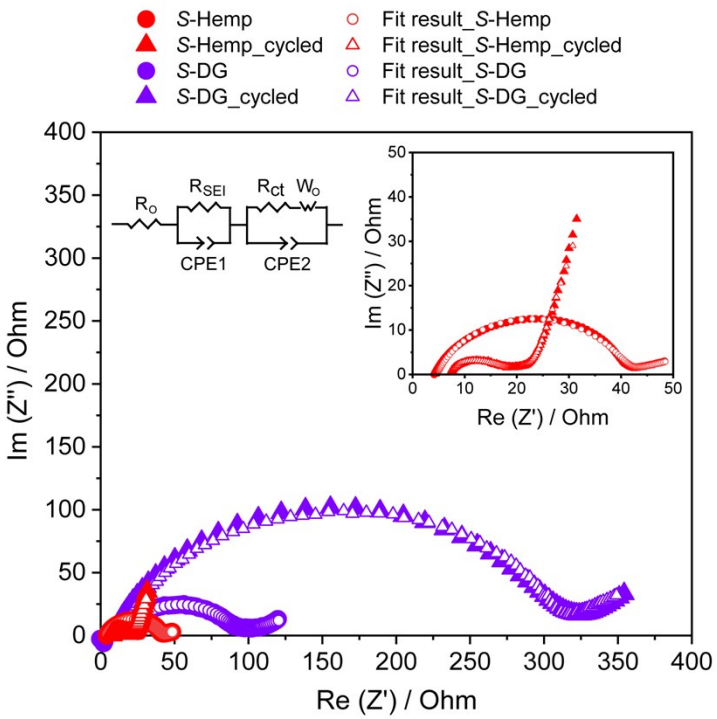

Fig. S5. The electrochemical impedance spectroscopy (EIS) of Li–S cell using *S*-Hemp (red symbol) and *S*-DG (purple symbol) electrodes, with the equivalent circuit described. The inset is the measured and fit result of *S*-Hemp and cycled *S*-Hemp.

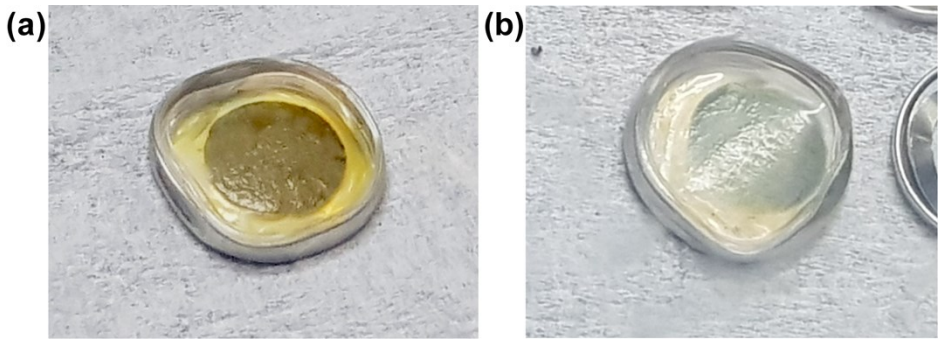

Fig. S6. Photographs of the disassembled Li–S coin cells. (a) The disassembled cell with *S*-DG cathode shows a yellow-dyed separator, while (b) the cell with *S*-Hemp demonstrates no color change due to the effective capturing of active materials.

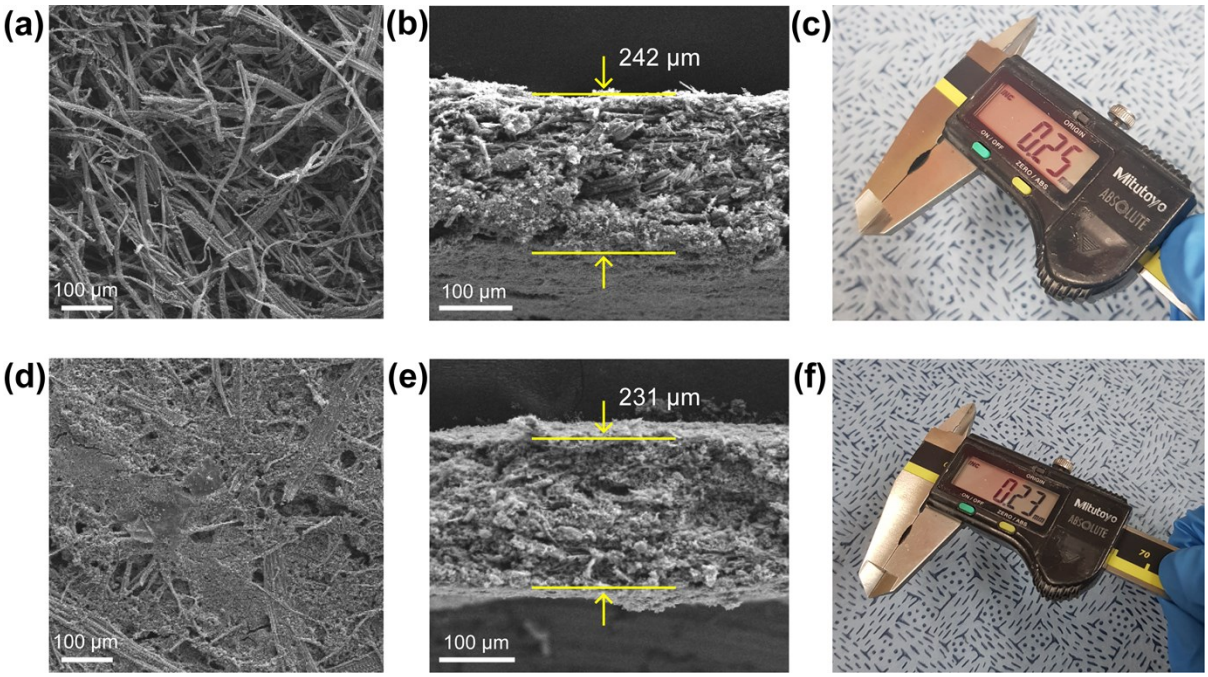

Fig. S7. Top- and cross-sectional view of the electrodes before and after cycling. (a) Top-view of the *C*-Hemp demonstrates the microstructure of interwoven carbon tubes. (b) Cross-sectional view of *C*-Hemp with the thickness of 242 µm. (c) Photograph of the thickness of *C*-Hemp measured by Vernier calipers. (d) Top-view of the *S*-Hemp after 50 cycles showing the void are filled with active materials. (e) Cross-sectional view of the cycled *S*-Hemp with the thickness of 231 µm. (f) Photograph of the thickness of *S*-Hemp measured by Vernier calipers.

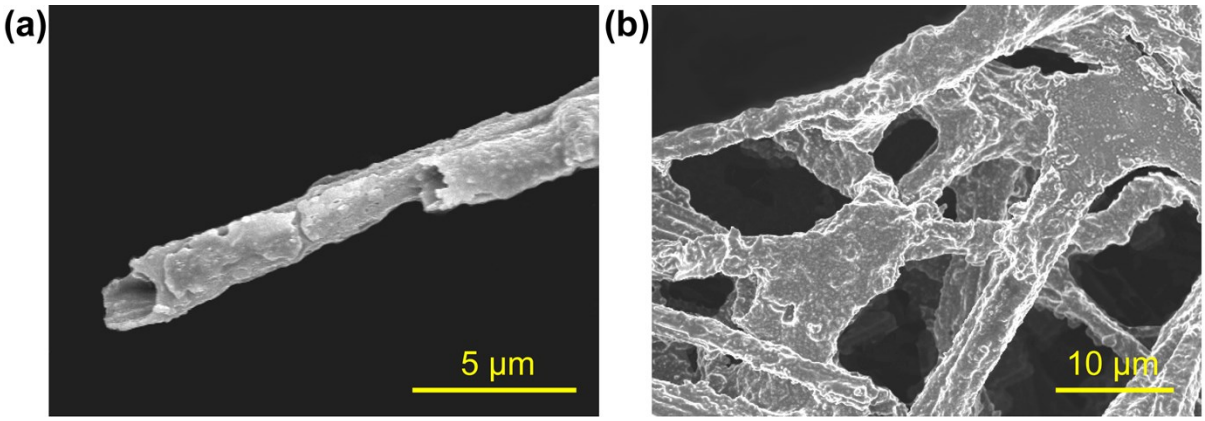

Fig. S8. SEM image of cycled *S*-Hemp electrode. (a) Deposition of sulfur-active material film onto the outer wall of *C*-Hemp after 5th cycling, and (b) accumulation of sulfur-active material in the interwoven space configured by the junction of fibers, as well as on the surface of the fibers, after 100th cycling.

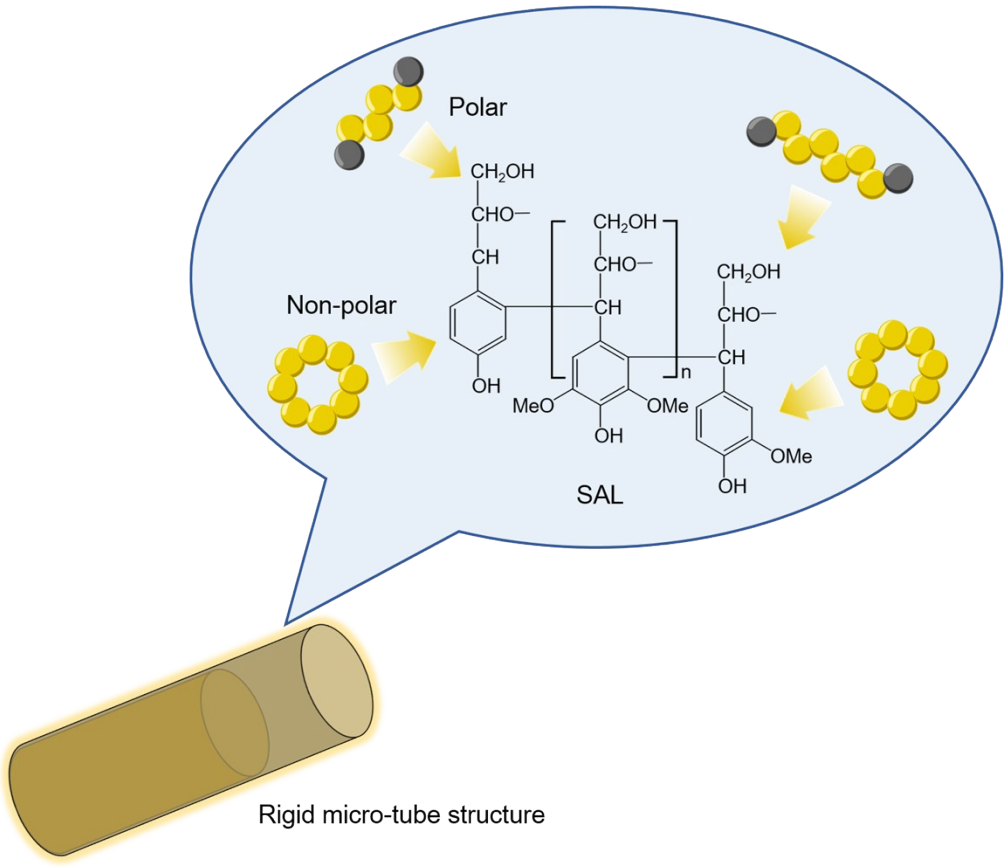

Fig. S9. Schematic illustration of the role of lignin in terms of structural integrity and facile utilization of active material.

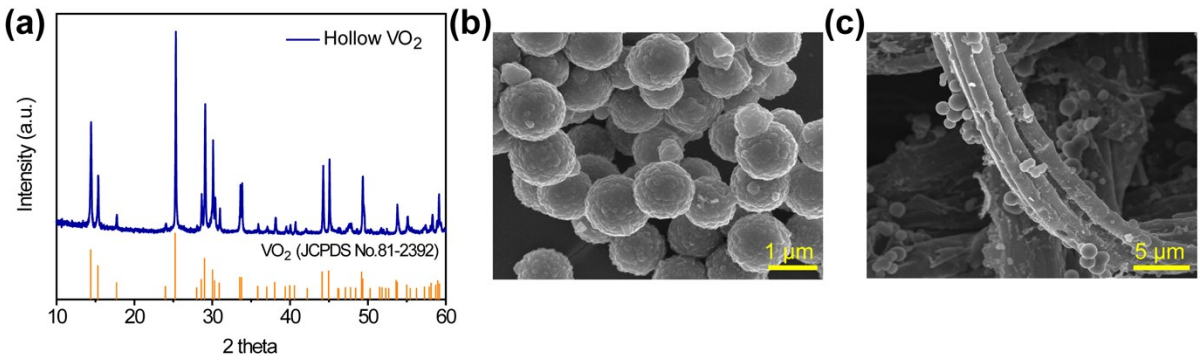

Fig. S10. XRD and SEM analysis of hollow VO_2. (a) XRD patterns and SEM images of (b) synthesized hollow VO_2 spheres and (c) VO_2-added *S*-Hemp electrode (*S*-Hemp@VO_2).

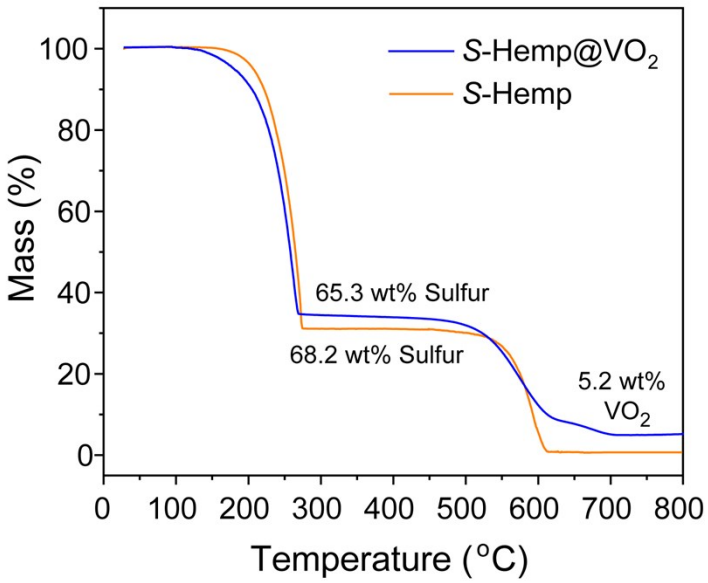

Fig. S11. Thermogravimetric analysis (TGA) of *S*-Hemp and *S*-Hemp@VO_2 electrodes.

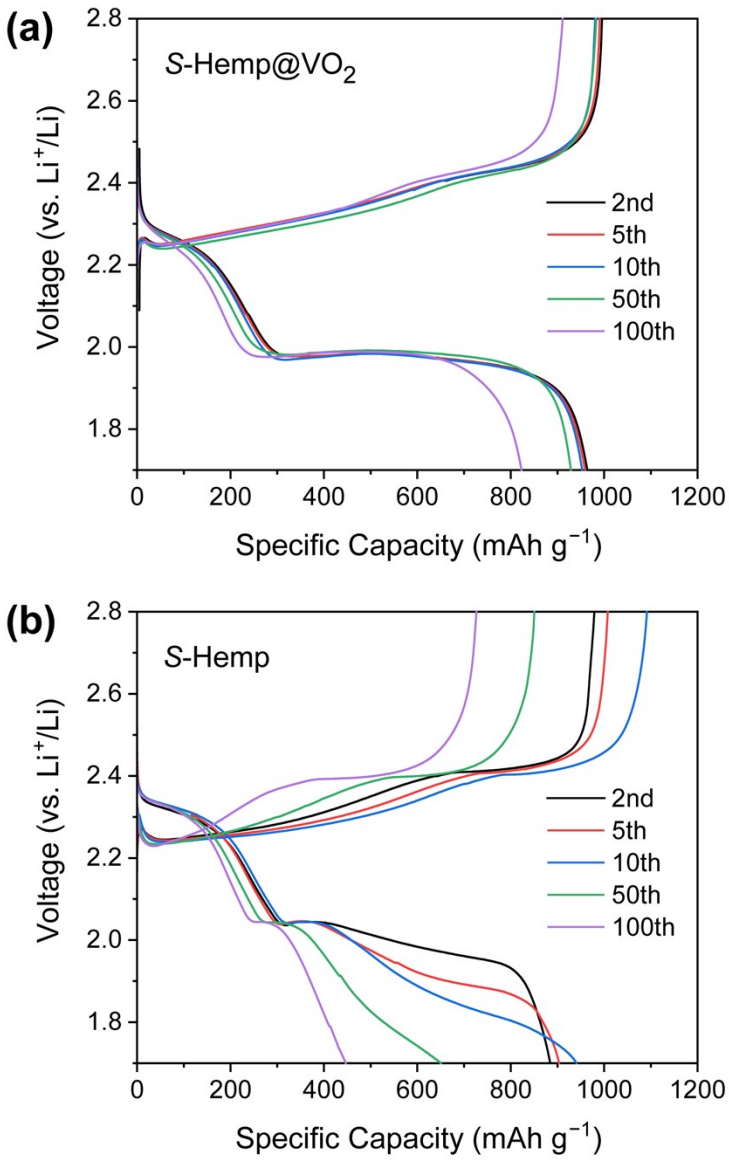

Fig. S12. The charge-discharge curves of the coin cell. (a) *S*-Hemp@VO_2 and (b) *S*-Hemp at 2nd, 5th, 10th, 50th, and 100th cycles, with a sulfur loading of 15.36 mg cm^{-2}. (0.1 C rate)

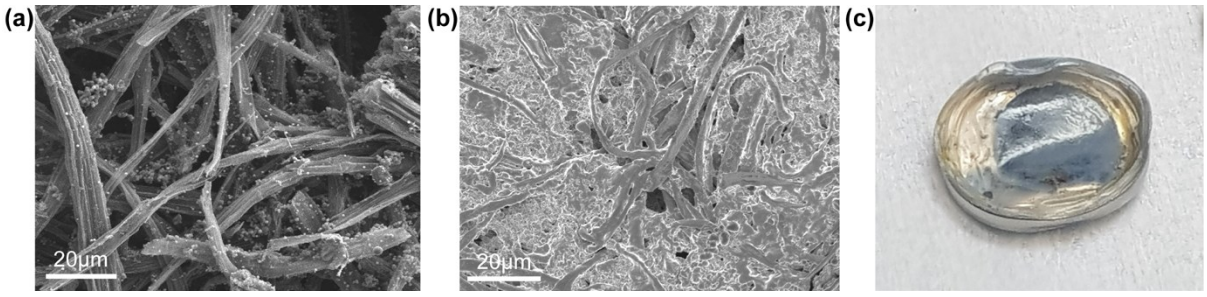

Fig. S13. Post-cycling characterization of the *S*-Hemp@VO_2 cathode. (a) Pristine *C*-Hemp@VO_2 cathode before cycling, demonstrating hollow VO_2-decorated carbon fibers. (b) The microstructure of the *S*-Hemp@VO_2 cathode after 100 cycles, and (c) the photograph of a disassembled cell showing no yellow-dyeing of the separator.

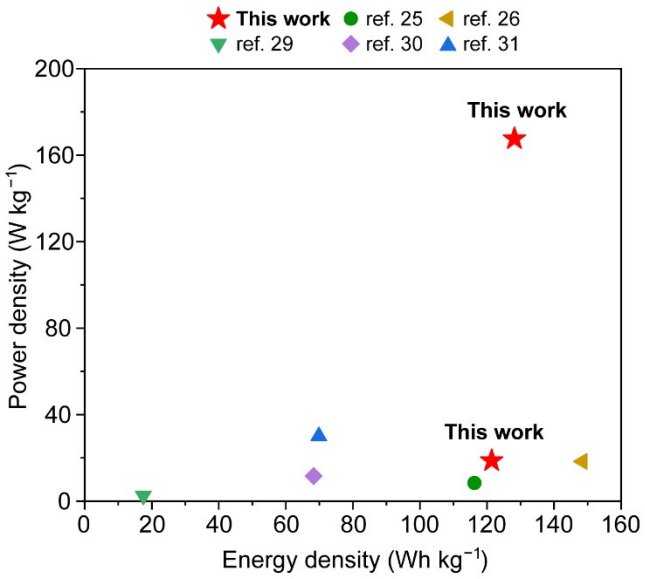

Fig. S14. Plots of Li−S cell performance based on carbonaceous fabrics as a function of energy density and power density. The performance metrics are listed in Table S6.

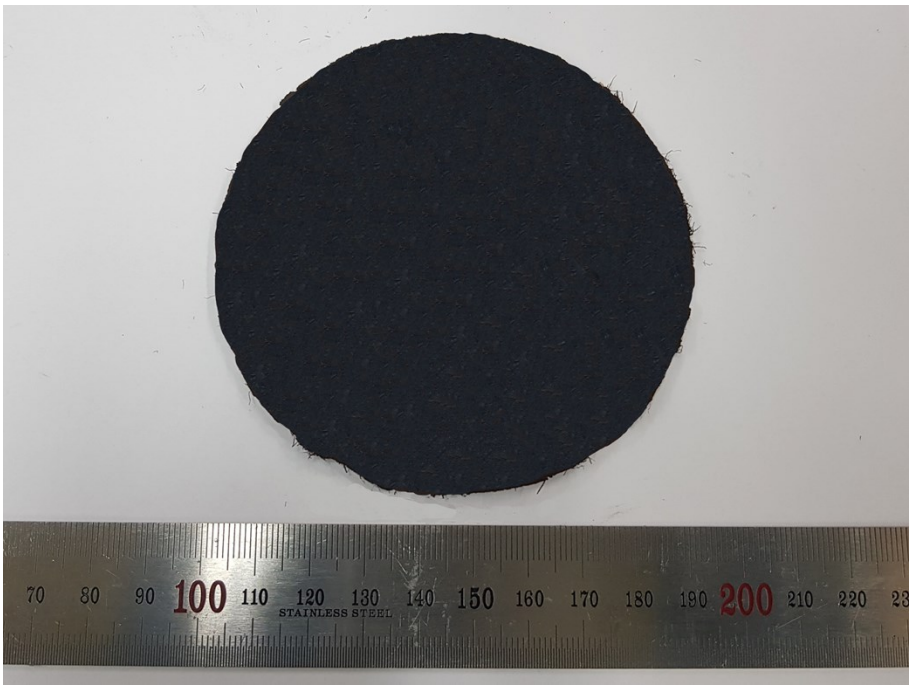

Fig. S15. Digital photograph of the self-assembled large-area *C*-Hemp sheet for the fabrication of pouch cell.

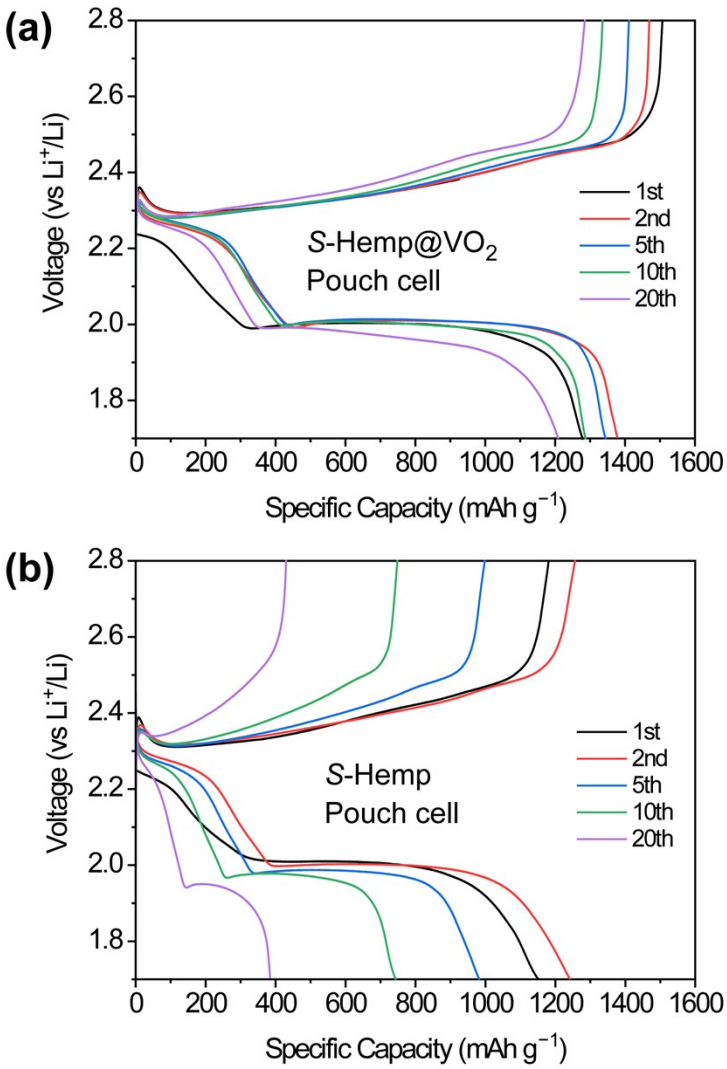

Fig. S16. The charge-discharge curves of the large-area (cathode area 12 cm^2) pouch cell. (a) *S*-Hemp@VO_2 and (b) *S*-Hemp with a sulfur loading of 5.12 mg cm^{-2} at 1st, 2nd, 5th, 10th, 20th cycles. (0.1 C rate)

Fig. S17. Digital photograph of the assembled operando Raman spectroscopy cell.

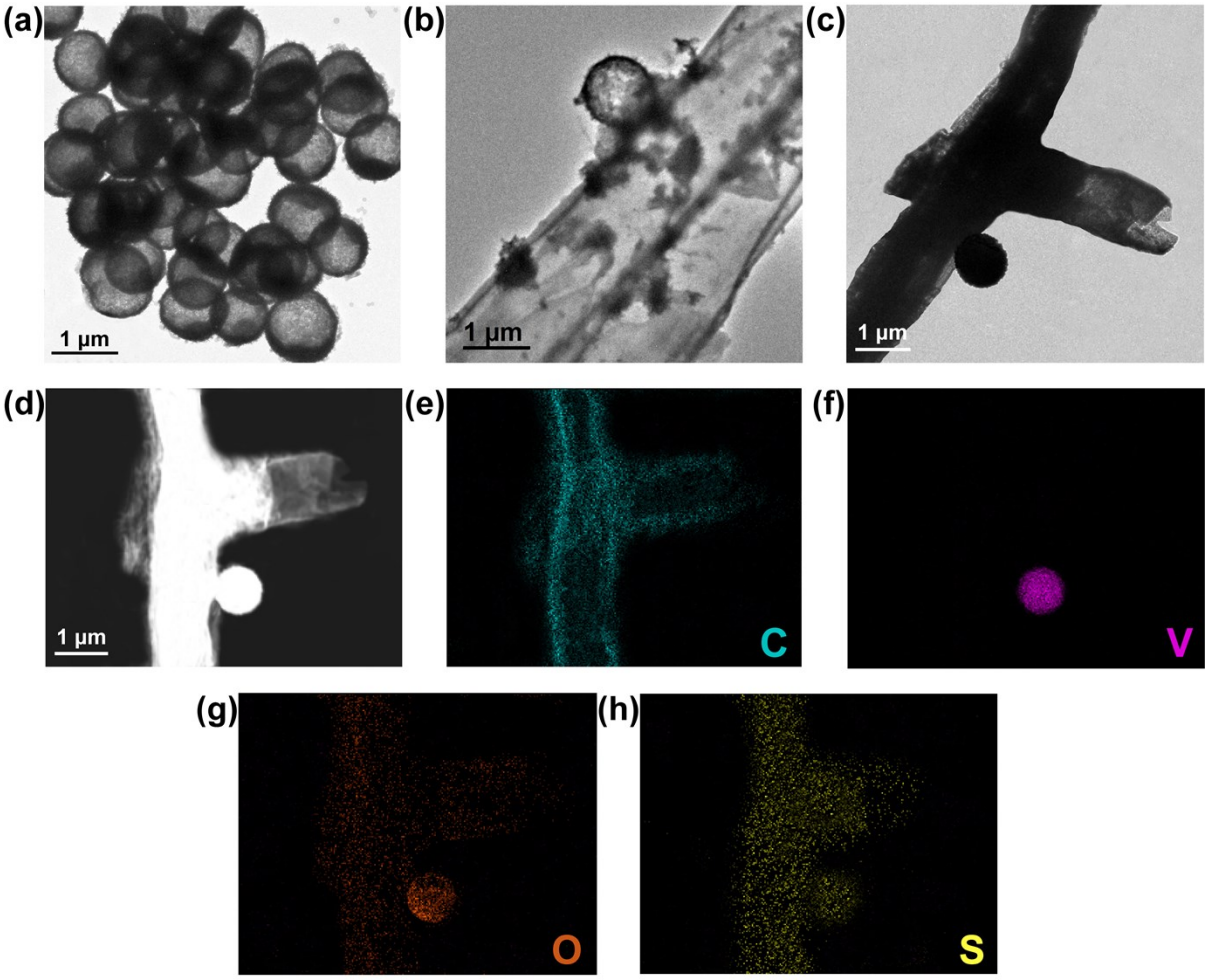

Fig. S18. TEM and STEM ex-situ analysis of *S*-Hemp@VO_2. Transmission electron microscopy (TEM) images of (a) hollow VO_2 spheres, (b) *S*-Hemp@VO_2 before cycling, and (c) *S*-Hemp@VO_2 after cycling. (d) Scanning transmission electron microscopy (STEM) image of cycled *S*-Hemp@VO_2, and its energy-dispersive X-ray spectroscopy (EDS) element mappings of (e) carbon, (f) vanadium, (g) oxygen, and (h) sulfur.